Millimeter-scale growth of YCrB₄ single crystals and observation of the metallic surface state

Xiaoni Zhang ⬤,[1] Yuki Tsujikawa ⬤,[1] Kazuki Yamaguchi,[1] Masashige Miyamoto ⬤,[1] Masafumi Horio ⬤,[1] Kunio Yubuta ⬤,[2] Hiroshi Ando ⬤,[1] Mei Yuan,[3] Kenichi Ozawa,[4] Kazumasa Sugiyama,[5] Takahiro Kondo,[3] and Iwao Matsuda ⬤[1]

[1]*Institute for Solid State Physics (ISSP), The University of Tokyo, Kashiwa, Chiba 277-8581, Japan*
[2]*Faculty of Engineering, Kyushu University, Fukuoka 819-0395, Japan*
[3]*Institute of Pure and Applied Sciences, University of Tsukuba, Tsukuba, Ibaraki 305-8573, Japan*
[4]*Institute of Materials Structure Science, KEK, Ibaraki 305-0801, Japan*
[5]*Institute for Materials Research, Tohoku University, Sendai 980-8577, Japan*

Millimeter-scale growth of YCrB₄ crystals was achieved by postannealing, followed by conventional arc melting. The bulk crystal was semiconducting, whereas the surface was metallic, as observed by photoemission spectroscopy. First-principles calculations consistently reproduced the metallicity in a model of the boron-terminated surface of the YCrB₄ crystal. These results support further investigations of different states on the surface of metal boride bulk materials.

I. INTRODUCTION

Metal borides receive significant attention for physics research and applications because of their beneficial material properties [1–4]. Recently, there has been particular interest in layered borides, which feature a two-dimensional (2D) boron network, sandwiched by layers of metal atoms. Notable examples are metal diborides (MB₂, where M denotes a metal) that exhibit unusual electronic properties, such as superconductivity [4,5]. Additionally, layered metal borides have been used for preparing various types of boron sheets [6]. Free-standing sheets of hydrogen boride (HB) have been synthesized by chemical exfoliation of metal boride crystals [5,7,8]. Concerning a borophene layer, it was found only on the ZrB₂ substrate [9], which is in contrast to rich reports on metal crystal surfaces, such as Ag, Cu, and Al [6,10,11].

YCrB₄ is one of the MB₂ crystal types that is composed of two different metal (M) atoms [12,13]. It possesses a layered borophene structure, which is a 2D boron network that comprises pentagons (five-membered rings) and heptagons (seven-membered rings) [5,14–18]. The crystal structure of YCrB₄ is illustrated in Fig. 1(a), and it belongs to the nonsymmorphic symmetry group. This unique crystal structure is useful for studying topological physics and the emergence of exotic electronic states or Dirac nodal lines after chemical treatment [5,19]. Because the YCrB₄ crystal inherently contains the 2D boron layer, the crystal surface can also serve as a platform to investigate borophene. However, the conventional method of arc melting typically yields microcrystals of YCrB₄ [5,20], as shown in Fig. 1(b). The product is also accompanied by impurities, typically minor crystals composed of the other borides. To examine the YCrB₄ surface properties, it is necessary to grow large-area single crystals.

In the present paper, we developed a method to grow acicular crystals of YCrB₄ that are over 1 mm long and 0.2–0.3 mm wide, as shown in Fig. 1(c), using a combination of the arc-melting and postannealing processes. The large area of the crystal allows surface science techniques, such as photoelectron spectroscopy (PES), to be applied after cleaning the sample by annealing and Ar sputtering. PES revealed that the surface is boron rich and has metallic states at the Fermi level. The first-principles calculation of the boron-terminated YCrB₄ surface consistently reproduced the gapless state of boron. These findings advance our comprehension of the YCrB₄ growth and surface properties, promoting further research in the fields of topological insulators and 2D materials.

II. METHODS

High-purity YCrB₄ crystals were grown based on the conventional arc-melting method [5,21]. Yttrium (Y, >99.9%), chromium (Cr, >99.999%), and boron (B, >99.5%) were loaded into a copper hearth and melted under an argon (Ar) atmosphere. The resulting sample was remelted three times to ensure homogeneity. Single crystals of YCrB₄ were obtained by synthesis using the atomic ratio of Y : Cr : B = 1 : 1 : 4 or by cutting from the as-cast samples, which have the ratio of Y : Cr : B = 1 : 18 : 4.

The quality of the single crystals was evaluated by x-ray diffraction (XRD) and x-ray photoelectron spectroscopy (XPS). The powder XRD measurements were conducted using a SmartLab 3-kW instrument operating with the Cu $K\alpha$ line or a Rigaku XtaLAB Synergy diffractometer with the Mo $K\alpha$ line. Analyses of the XRD data were performed using the reference intensity ratio (RIR) method [22,23] and the *CrysAlis PRO* software package [24]. Single-crystal XRD experiments were conducted using a Rigaku XtaLAB Synergy diffractometer. The XPS experiments were performed at the beamline BL-13B in the Photon Factory at the High Energy Accelerator Research Organization (KEK) [25].

The electronic structure of the metal boride crystals was calculated using density functional theory (DFT) with the QUANTUM ESPRESSO code [26]. Spin-orbit coupling was neglected, and the generalized gradient approximation with
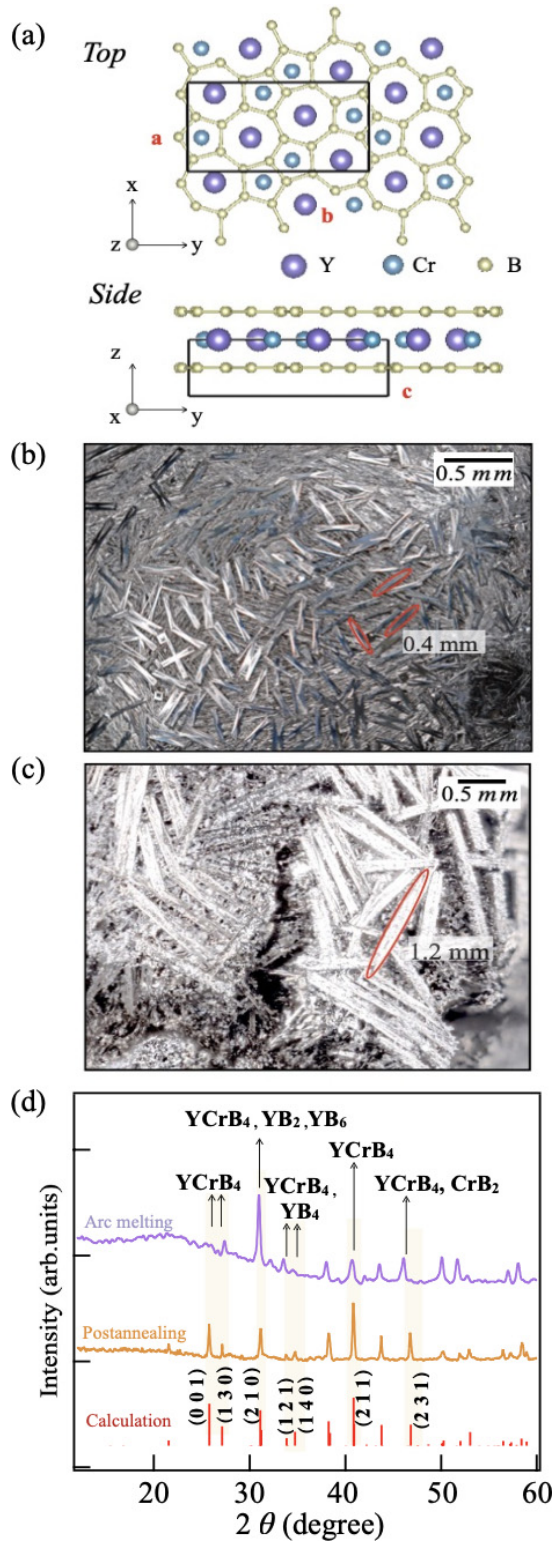
FIG. 1. (a) Illustration of the YCrB$_4$ atomic structure, showing a two-dimensional boron network featuring pentagons (five-membered rings) and heptagons (seven-membered rings) sandwiched between rare-earth metal (Y) and transition-metal (Cr) layers. (b), (c) Optical microscopy images of the YCrB$_4$ samples prepared by (b) arc melting and (c) arc melting with the postannealing process. (d) Comparison of the powder x-ray diffraction patterns for YCrB$_4$ crystals after arc melting (purple) and postannealing (yellow), and the calculated pattern for the YCrB$_4$ crystal (red).

nonrelativistic Perdew-Burke-Ernzerhof parametrization was used for the exchange-correlation term [27]. Valence-wave functions were expanded using a plane-wave basis, and the cutoff energies were set at 60 and 360 Ry for the wave functions and charge density, respectively. The k-point grid on the Brillouin zone was taken at $8 \times 4 \times 16$ in the band calculations. Parameters of the YCrB$_4$ unit cells were taken as $a = 5.875\,19$ Å, $b = 11.292\,08$ Å, and $c = 3.525\,11$ Å, which were optimized from experimental values and corresponded to the previous report [15]. For the surface calculation, a vacuum region of 15 Å was used to separate the periodic images. The Perdew-Burke-Ernzerhof functional for solids was used as pseudopotentials [27].

III. RESULTS AND DISCUSSIONS

A. Preparation and characterization of the millimeter-sized YCrB$_4$ single crystal

Figure 1(b) shows an optical microscopy image of the YCrB$_4$ crystals grown by arc melting with the ratio of Y : Cr : B = 1 : 1 : 4. The surface of the sample is covered with needlelike or acicular single crystals, with lengths of approximately 0.4 mm. The XRD results given in Fig. 1(d) reveal the characteristic Bragg peaks, confirming the crystallinity. In addition, the resistivity of the YCrB$_4$ sample was measured in the temperature range of 2–150 K using a physical properties measurement system, confirming the semiconducting properties of the bulk crystal, as previously reported [16–18].

The bulk YCrB$_4$ crystal [Fig. 1(b)] subsequently underwent a postannealing process at 1450 °C for 7 days under an Ar atmosphere, with a temperature ramp of approximately 60 °C/h. Subsequently, the crystal was gradually cooled from 1450 °C to room temperature, employing a temperature ramp of 20 °C/h. An optical microscopy image of the resulting sample is presented in Fig. 1(c). The size of the acicular YCrB$_4$ crystals increased to 1.2 mm in length, with a wider average width. Note that cracks are also observed at the sample surface. The XRD results in Fig. 1(d) indicate that the crystallinity of the sample improved after the postannealing process. Initial YCrB$_4$ samples fabricated by arc melting exhibited broad features and lacked several Bragg peaks that were expected from the calculation, especially in the range of $2\theta = 20°–30°$. Diffraction peaks emerged at (001) ($2\theta = 25.6°$) and (211) ($2\theta = 40.6°$) for the YCrB$_4$ crystalline structure after postannealing. Additionally, the peaks at $2\theta = 31°$ and 46°, originating from minor phases, such as CrB$_2$, YB$_2$, YB$_4$, and YB$_6$ [5,7], are reduced. Compositional analysis was conducted based on the XRD data for the samples before and after the postannealing process. The crystallite size was determined by calculating the full width at half maxima values obtained from the XRD spectra using the Scherrer formula. Specifically, for the peak of the (211) orientation, the crystallite size increased from 19 to 35 nm. Table I summarizes the average yields of the YCrB$_4$ samples obtained by arc melting and postannealing. The yields were calculated using the RIR method. There was a significant increase in the average yield (%) by postannealing, with a decrease in the standard deviation.

TABLE I. Yield(%) of $YCrB_4$ obtained by arc melting and postannealing.

Components	$YCrB_4$	CrB_2	YB_2	YB_4	YB_6
After arc-melting process					
Average	65.0	13.1	12.3	4.4	5.2
Standard deviation	21.8	13.7	16.4	6.17	10.2
After postannealing process					
Average	92.2	3.1	1.7	1.5	1.5
Standard deviation	2.3	2.7	1.1	1.3	1.0

The changes in the XRD data reveal the purification of the $YCrB_4$ crystal by reducing possible impurities (metallic oxides) and increasing the homogeneity of local crystal structures. The significant enlargement of the crystal size implies that remelting of the $YCrB_4$ crystals has occurred during the postannealing process at 1450 °C. While the melting temperature has not been reported for $YCrB_4$ under the given atmospheric conditions, the present results indicate that the melting point is below 1450 °C.

Moreover, single-crystal XRD was performed on 0.05 mm × 0.02 mm × 0.02 mm samples cut from the as-cast single crystals. Figure 2 shows reciprocal space sections reconstructed from the single-crystal XRD results: in Fig. 2(a) $(hk0)^*$ and in Fig. 2(b) $(h0l)^*$ reciprocal planes. Based on the reconstructed reciprocal space section for $(hk0)^*$ [Fig. 2(a)], the $YCrB_4$ single crystal contains twin structure variants of the $YCrB_4$-type phase. The twin-related variants exist on the atomic arrangement level. The rectangle reciprocal lattices represented in red and blue in Fig. 2 are based on the unit cells taken from the original and twin-related variants, respectively. The overlapping diffraction spots enclosed by a circle in Fig. 2(a) indicate that the crystallographic relationship between the original and twin variants can be expressed as $(0\bar{4}0)_{original}[001] \| (2\bar{1}0)_{twin}[001]$. On the other hand, there is no sign of the twin-related variants on the $(0kl)^*$ reciprocal plane, as shown in Fig. 2(b).
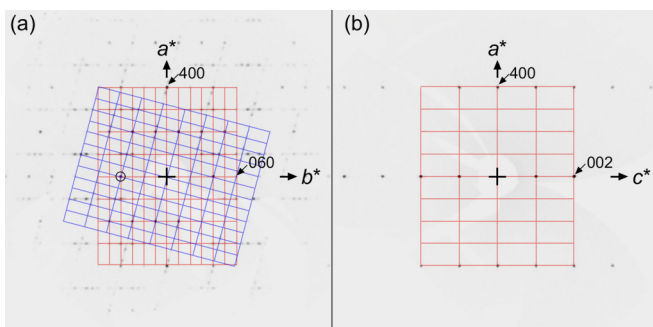
FIG. 2. Reciprocal space sections reconstructed from the single-crystal XRD results: (a) $(hk0)^*$ and (b) $(h0l)^*$ reciprocal planes. The twin-related variants exist on the atomic arrangement level. The rectangle reciprocal lattices represented in red and blue are based on the unit cells of the original and twin-related variants, respectively.
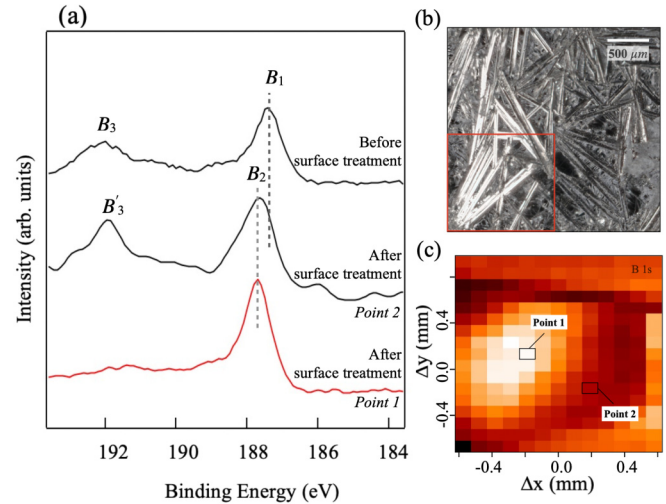
FIG. 3. (a) A collection of B 1s core-level photoemission spectra for the $YCrB_4$ crystal, obtained before and after cleaning treatment of the sample surface. Spectra labeled points 1 and 2 were taken at the positions indicated in (c). The spectra were taken at $h\nu = 285$ eV. (b) Optical microscopy image of the $YCrB_4$ crystal after surface treatment for the PES measurement. (c) Spatial mapping of the photoemission intensity integrated over the E_B range of 186–190 eV, measured with $h\nu = 650$ eV. The step size was 100 μm along the x and y directions. The region corresponds to the area indicated by the red square in (a). All measurements were performed at room temperature

B. Surface analysis of the YCrB₄ crystal

Millimeter-scale growth of the high-purity $YCrB_4$ crystal was observed in this study, providing a wide sample area for surface analysis. Notably, synchrotron radiation beamlines have been developed to probe the submillimeter region using microfocused x-ray beams. Herein, the $YCrB_4$ sample, Fig. 1(c), was installed in the end station of the KEK-PF BL-13B beamline, and PES measurement was performed. Figure 3(a) presents a collection of the B 1s core-level spectra of the $YCrB_4$ surface, obtained under different conditions. A spectrum of the crystal transferred in air shows two prominent peaks at the binding energies of 187.3 eV (B_1) and 192.0 eV (B_3), which are assigned to the internal boron atoms in the bulk and the boron oxides at the surface, respectively [20].

Adopting the conventional process of surface cleaning, the $YCrB_4$ surface underwent repeated cycles of Ar^+ ion-bombardment sputtering (1.5 kV for 30 min) and high-temperature annealing (700 °C for 3 h). After the treatment, a new peak, B_2, emerges at the binding energy of 187.7 eV. Note that the observed boron peaks (B_1 and B_2) are ascribed to negatively charged boron, as previously reported [28]. The presence of the boron oxide peak (B_3') depends on measurement positions at the surface. Figure 3(b) shows an optical microscopy image of the sample surface, and Fig. 3(c) shows a spatial map of the photoemission intensity for the boron peaks (B_1 and B_2) in the binding energy range of 186–190 eV. The region in Fig. 3(c) corresponds to the partial region in Fig. 3(b), as indicated by the red square that covers several acicular crystals of $YCrB_4$. In the area with the relatively large peak intensity, the position labeled as point 1 contains a sharp
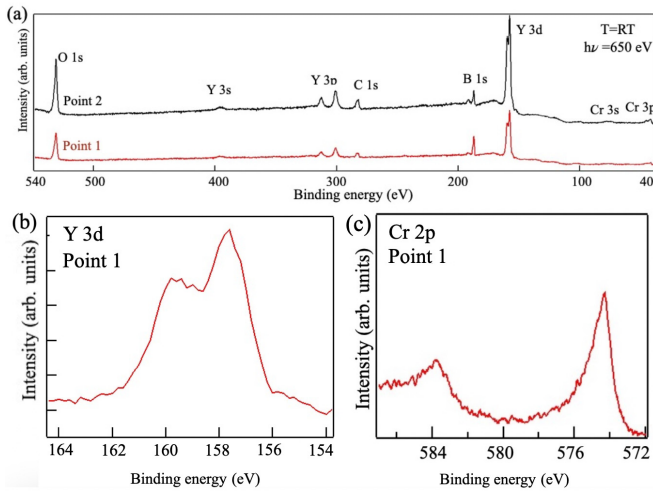
FIG. 4. (a) Photoemission spectra of the YCrB$_4$ crystal after surface treatment at point 1 and 2 indicated in Fig. 3(c), obtained in the binding energy range of 40–540 eV with $hv = 650$ eV. (b), (c) Core-level spectra of the (b) Y 3d and (c) Cr 2p orbitals, measured at the point 1 with $hv = 650$ eV.

B_2 peak and a negligible contribution from the boron oxide [Fig. 3(a)]. Conversely, the appearance of the boron oxide peak (B'_3) at 192 eV is notable in the spectrum at point 2, whereas the B 1s peak intensity is relatively small [Fig. 3(a)]. At point 2, the peak at a binding energy of 187.6 eV has a wide spectral width, suggesting contributions from both the B_1 and B_2 components. Comparing the images in Figs. 3(b) and 3(c), Point 1 corresponds to the acicular single crystal, and the B_2 peak is naturally assigned to the YCrB$_4$ surface component that has a different chemical environment from the internal bulk B_1. The absence of the B'_3 peak indicates the elimination of boron oxides from the crystal surface.

Points 1 and 2 were further analyzed by XPS, as shown in Fig. 4(a). The spectra show the main elements (Y, Cr, B) of YCrB$_4$ and the surface impurity elements (C, O) at the corresponding binding energies. The amount of oxygen impurities is smaller at point 1 than at point 2. The absence of the boron oxide peak in the B 1s core-level spectrum at point 1 indicates that the oxygen species originates from the metal oxides. Notably, as depicted in Fig. 4(a), the intensities of Y and Cr at point 1 are smaller than those at point 2, whereas the boron peak is enhanced. This suggests that point 1 corresponds to a relatively boron-rich area, indicating the potential existence of a B-terminated surface.

C. Electronic structure at the YCrB$_4$ surface

Next, the valence-band photoemission spectra were captured at point 1 before and after the surface cleaning treatment (sputtering and annealing). Figure 5 displays the energy distribution curves (EDCs) obtained with a photon energy of $hv = 187$ eV. Before surface treatment, the curve shows an apparent energy gap at the Fermi level (E_F). The spectral features likely represent the bulk states of the YCrB$_4$ crystal, which are semiconducting [5,20]. After surface cleaning, a gapless state was observed as an edge at E_F, indicating a metallic nature. This indicates the emergence of the metal-
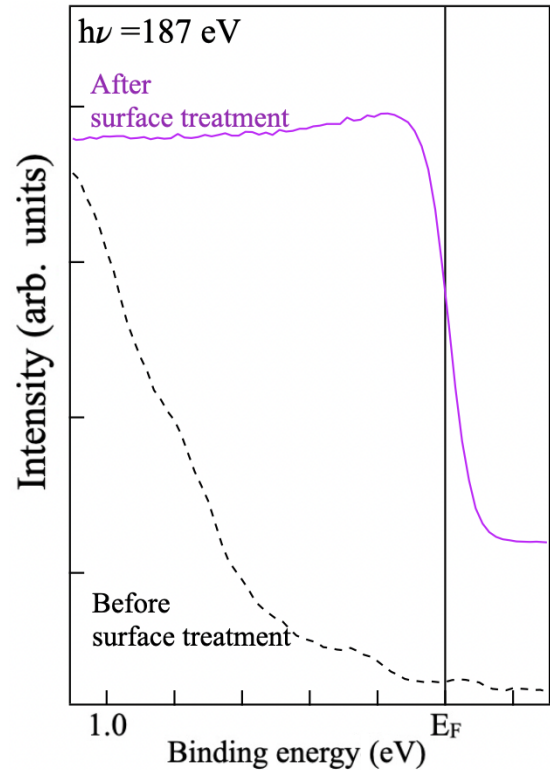
FIG. 5. EDCs with photon energy $hv = 187$ eV at point 1, before (black dashed line) and after (purple line) cleaning the surface. EDCs of the spectra were calibrated using the Fermi edge of an Au reference sample at the corresponding incident photon energy and normalized to the photon flux. The measurement was performed at 50 K.

lic surface on the semiconducting crystal. Because the clean surface is boron rich, as identified in Fig. 3, the metallicity is likely related to a borophene layer at the surface.

Considering that point 1 corresponds to the boron-rich region, as shown in Fig. 3(c), we conclude that the surface is terminated by boron. To examine the boron layer, the electronic band structure of the YCrB$_4$ crystal was calculated in a DFT framework. A model of the B-terminated YCrB$_4$ surface was illustrated using VESTA [29], as given in Fig. 6(a). Figure 6(c) shows the calculated band structure of YCrB$_4$ with an optimized B-terminated surface. The electronic behavior of the boron surface layer differs from the semiconducting properties of the bulk YCrB$_4$ crystal [5]. In addition, the partial density of states analysis of the bands indicates that the gapless state is composed of boron orbitals. These results are consistent with the experimental observation of the metallic state at the Fermi level, as given in Fig. 5. These facts indicate that the boron-terminated surface is formed after cleaning the YCrB$_4$ crystal surface, and the new surface state is metallic.

The surfaces of metal borides are regarded as ideal platforms for the formation of metallic borophene. One significant example is ZrB$_2$, which exhibits graphenelike borophene on the surface [9], displaying distinctive band features compared with its bulk state [30]. Another notable example is MgB$_2$, where distinctive features are observed in the bulk and Mg-terminated surface [31]. While discussions concerning RMB$_4$ [rare-earth metals (R) and transition metals (M)] borides have
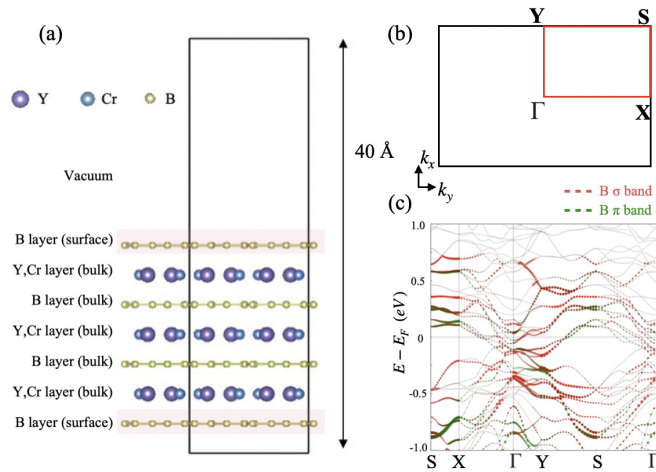
FIG. 6. (a) A model of the B-terminated (001) surface of $YCrB_4$. (b) Two-dimensional Brillouin zone of the (001) surface. (c) $YCrB_4$ (001) surface band calculation based on the model depicted in (a).

primarily focused on bulk states [32,33], our findings provide interesting insights into their surface properties.

Although the surface reconstruction can potentially be observed by electron diffraction and angle-resolved photoemission spectroscopy, it is highly challenging. This difficulty arises from the presence of yttrium oxide [Fig. 4(b)] and other possible impurities, reducing the surface flatness. In addition, employing a higher annealing temperature ($>1500\,°C$) could be a viable strategy to enhance surface flatness; however, this requires a specialized heating environment in an ultrahigh vacuum chamber.

IV. SUMMARY

In summary, we report the growth of millimeter-sized $YCrB_4$ crystals by arc melting and postannealing. Although the bulk $YCrB_4$ crystal is known to be semiconducting, we found that the surface is metallic, as observed by PES. The surface is boron rich, and the gapless state at the Fermi level was consistently reproduced by the first-principles calculation of the boron-terminated surface. The $YCrB_4$ crystal surface is likely covered with a metallic layer of borophene. These findings offer unique insights and promote the preparation and investigation of 2D layers using 3D metal borides.

[1] W. N. Kang, H.-J. Kim, E.-M. Choi, C. U. Jung, and S.-I. Lee, Science **292**, 1521 (2001).

[2] B. Ganem and J. O. Osby, Chem. Rev. **86**, 763 (1986).

[3] J. P. Scheifers, Y. Zhang, and B. P. T. Fokwa, Acc. Chem. Res. **50**, 2317 (2017).

[4] H. J. Choi, D. Roundy, H. Sun, M. L. Cohen, and S. G. Louie, Nature (London) **418**, 758 (2002).

[5] X. Zhang, Y. Tsujikawa, I. Tateishi, M. Niibe, T. Wada, M. Horio, M. Hikichi, Y. Ando, K. Yubuta, T. Kondo, and I. Matsuda, J. Phys. Chem. C **126**, 12802 (2022).

[6] I. Matsuda and K. Wu, *2D Boron: Boraphene, Borophene, Boronene* (Springer, New York, 2021).

[7] X. Zhang, M. Hikichi, T. Iimori, Y. Tsujikawa, M. Yuan, M. Horio, K. Yubuta, F. Komori, M. Miyauchi, T. Kondo, and I. Matsuda, Molecules **28**, 2985 (2023).

[8] H. Nishino, T. Fujita, N. T. Cuong, S. Tominaka, M. Miyauchi, S. Iimura, A. Hirata, N. Umezawa, S. Okada, E. Nishibori *et al.*, J. Am. Chem. Soc. **139**, 13761 (2017).

[9] S. Suehara, T. Aizawa, and T. Sasaki, Phys. Rev. B **81**, 085423 (2010).

[10] B. Feng, O. Sugino, R.-Y. Liu, J. Zhang, R. Yukawa, M. Kawamura, T. Iimori, H. Kim, Y. Hasegawa, H. Li, L. Chen, K. Wu, H. Kumigashira, F. Komori, T.-C. Chiang, S. Meng, and I. Matsuda, Phys. Rev. Lett. **118**, 096401 (2017).

[11] W. Li, L. Kong, C. Chen, J. Gou, S. Sheng, W. Zhang, H. Li, L. Chen, P. Cheng, and K. Wu, Sci. Bull. **63**, 282 (2018).

[12] I. Veremchuk, T. Mori, Y. Prots, W. Schnelle, A. Leithe-Jasper, M. Kohout, and Y. Grin, J. Solid State Chem. **181**, 1983 (2008).

[13] C. Benndorf, M. de Oliveira, C. Doerenkamp, F. Haarmann, T. Fickenscher, J. Kösters, H. Eckert, and R. Pöttgen, Dalton Trans. **48**, 1118 (2019).

[14] Y. B. Kuz'ma, Kristallografiya **15**, 372 (1970).

[15] P. Rogl, Mater. Res. Bull. **13**, 519 (1978).

[16] J. Simonson and S. Poon, J. Alloys Compd. **504**, 265 (2010).

[17] S. Flipo, H. Rosner, M. Bobnar, K. O. Kvashnina, A. Leithe-Jasper, and R. Gumeniuk, Phys. Rev. B **103**, 195121 (2021).

[18] N. I. Medvedeva, Y. E. Medvedeva, and A. L. Ivanovskii, Dokl. Phys. Chem. **383**, 75 (2002).

[19] N. T. Cuong, I. Tateishi, M. Cameau, M. Niibe, N. Umezawa, B. Slater, K. Yubuta, T. Kondo, M. Ogata, S. Okada, and I. Matsuda, Phys. Rev. B **101**, 195412 (2020).

[20] M. Niibe, M. Cameau, N. T. Cuong, O. I. Sunday, X. Zhang, Y. Tsujikawa, S. Okada, K. Yubuta, T. Kondo, and I. Matsuda, Phys. Rev. Mater. **5**, 084007 (2021).

[21] M. Tokuda, K. Yubuta, T. Shishido, and K. Sugiyama, Acta Crystallogr., Sect. E: Crystallogr. Commun. **79**, 1072 (2023).

[22] C. R. Hubbard, E. H. Evans, and D. K. Smith, J. Appl. Crystallogr. **9**, 169 (1976).

[23] R. L. Snyder, Powder Diffr. **7**, 186 (1992).

[24] Rigaku Oxford Diffraction Ltd., Yarnton, England, Rigaku oxford diffraction: CrysAlisPro, (2018), https://www.rigaku.com/products/crystallography/crysalis.

[25] A. Toyoshima, T. Kikuchi, H. Tanaka, K. Mase, K. Amemiya, and K. Ozawa, J. Phys.: Conf. Ser. **425**, 152019 (2013).

[26] P. Giannozzi, S. Baroni, N. Bonini, M. Calandra, R. Car, C. Cavazzoni, D. Ceresoli, G. L. Chiarotti, M. Cococcioni, I. Dabo, A. D. Corso, S. de Gironcoli, S. Fabris, G. Fratesi, R. Gebauer, U. Gerstmann, C. Gougoussis, A. Kokalj, M. Lazzeri, L. Martin-Samos *et al.*, J. Phys.: Condens. Matter **21**, 395502 (2009).

[27] J. P. Perdew, K. Burke, and M. Ernzerhof, Phys. Rev. Lett. **77**, 3865 (1996).

[28] T. Kondo, Chem. Lett. **52**, 611 (2023).

[29] K. Momma and F. Izumi, J. Appl. Crystallogr. **44**, 1272 (2011).

[30] R. Lou, P. Guo, M. Li, Q. Wang, Z. Liu, S. Sun, C. Li, X. Wu, Z. Wang, Z. Sun, D. Shen, Y. Huang, K. Liu, Z.-Y. Lu, H. Lei, H. Ding, and S. Wang, npj Quantum Mater. **3**, 43 (2018).

[31] S. Souma, Y. Machida, T. Sato, T. Takahashi, H. Matsui, S.-C. Wang, H. Ding, A. Kaminski, J. C. Campuzano, S. Sasaki, and K. Kadowaki, Nature (London) **423**, 65 (2003).

[32] Y. Han, Y. Shang, W. Wan, Y. Liu, and Y. Ge, New J. Phys. **25**, 103019 (2023).

[33] N. Pakhira, J. Krishna, S. Nandy, T. Maitra, and A. Taraphder, arXiv:1807.05388.